



# Graphene-based tunable ultra-narrowband mid-infrared TE-polarization absorber

YAN-LIN LIAO<sup>1</sup> AND YAN ZHAO<sup>2,\*</sup>

<sup>1</sup>*Key Laboratory of Intelligent Computing & Signal Processing, Ministry of Education, Anhui University, Hefei, 230039, China*

<sup>2</sup>*Department of Physics, Anhui Medical University, Hefei, 230032, China*

\*zhaoyan@ahmu.edu.cn

**Abstract:** A graphene-based tunable ultra-narrowband mid-infrared TE-polarization absorber is proposed. The simulation results show that, the absorption peak can be tuned from  $5.43896\mu\text{m}$  to  $5.41418\mu\text{m}$ , by tuning the Fermi level of graphene from 0.2eV to 1.0eV. The simulation results also show that the absorption bandwidth is less than 1.0nm and the absorption rate is more than 0.99 for TE-polarization (electric field is parallel to grating grooves) in the tuning wavelength range. The ultra-narrowband absorption mechanism is originated from the low power loss in the guided-mode resonance. The tuning function is mainly attributed to the change of the real part of the graphene's permittivity. This tunable ultra-narrowband mid-infrared absorber has potential applications in the tunable filtering and tunable coherent emission of thermal source.

© 2017 Optical Society of America under the terms of the [OSA Open Access Publishing Agreement](#)

**OCIS codes:** (300.1030) Absorption; (050.2770) Gratings; (260.5740) Resonance.

## References and links

1. N. Liu, M. Mesch, T. Weiss, M. Hentschel, and H. Giessen, "Infrared perfect absorber and its application as plasmonic sensor," *Nano Lett.* **10**(7), 2342–2348 (2010).
2. M. Diem, T. Koschny, and C. M. Soukoulis, "Wide-angle perfect absorber/thermal emitter in the terahertz regime," *Phys. Rev. B* **79**(3), 033101 (2009).
3. Y. Wang, T. Sun, T. Paudel, Y. Zhang, Z. Ren, and K. Kempa, "Metamaterial-plasmonic absorber structure for high efficiency amorphous silicon solar cells," *Nano Lett.* **12**(1), 440–445 (2012).
4. W. Cai, U. K. Chettiar, A. V. Kildishev, and V. M. Shalaev, "Optical cloaking with metamaterials," *Nat. Photonics* **1**(4), 224–227 (2007).
5. J. Rosenberg, R. V. Shenoi, T. E. Vandervelde, S. Krishna, and O. Painter, "A multispectral and polarization-selective surface-plasmon resonant midinfrared detector," *Appl. Phys. Lett.* **95**(16), 161101 (2009).
6. Y. Q. Xu, P. H. Zhou, H. B. Zhang, L. Chen, and L. J. Deng, "A wide-angle planar metamaterial absorber based on split ring resonator coupling," *J. Appl. Phys.* **110**(4), 044102 (2011).
7. Y. Wang, B. S. Liu, R. B. Bian, W. Z. Mao, C. X. Liu, B. Ma, and L. Chen, "A novel ultrathin and broadband microwave metamaterial absorber," *J. Appl. Phys.* **116**(9), 094504 (2014).
8. D. Y. Shchegolkov, A. K. Azad, J. F. O'Hara, and E. I. Simakov, "Perfect subwavelength fishnetlike metamaterial-based film terahertz absorbers," *Phys. Rev. B* **82**(20), 205117 (2010).
9. J. Grant, Y. Ma, S. Saha, L. B. Lok, A. Khalid, and D. R. S. Cumming, "Polarization insensitive terahertz metamaterial absorber," *Opt. Lett.* **36**(8), 1524–1526 (2011).
10. J. Hao, J. Wang, X. Liu, W. J. Padilla, L. Zhou, and M. Qiu, "High performance optical absorber based on a plasmonic metamaterial," *Appl. Phys. Lett.* **96**(25), 251104 (2010).
11. W. Ma, Y. Wen, and X. Yu, "Broadband metamaterial absorber at mid-infrared using multiplexed cross resonators," *Opt. Express* **21**(25), 30724–30730 (2013).
12. M. Luo, S. Shen, L. Zhou, S. Wu, Y. Zhou, and L. Chen, "Broadband, wide-angle, and polarization-independent metamaterial absorber for the visible regime," *Opt. Express* **25**(14), 16715–16724 (2017).
13. H. Ullah, A. D. Khan, A. Ullah, I. Ullah, and M. Noman, "Plasmonic perfect absorber for solar cell applications," in *2016 International Conference on Emerging Technologies* (IEEE, 2016), pp. 1–5.
14. P. Rufangura and C. Sabah, "Design and characterization of a dual-band perfect metamaterial absorber for solar cell applications," *J. Alloys Compd.* **671**, 43–50 (2016).
15. K. I. Bolotin, K. J. Sikes, Z. Jiang, M. Klima, G. Fudenberg, J. Hone, P. Kim, and H. L. Stormer, "Ultrahigh electron mobility in suspended graphene," *Solid State Commun.* **146**(9–10), 351–355 (2008).
16. B. Fallahazad, S. Kim, L. Colombo, and E. Tutuc, "Dielectric thickness dependence of carrier mobility in graphene with HfO<sub>2</sub> top dielectric," *Appl. Phys. Lett.* **97**(12), 123105 (2010).
17. K. S. Novoselov, V. I. Fal'ko, L. Colombo, P. R. Gellert, M. G. Schwab, and K. Kim, "A roadmap for graphene," *Nature* **490**(7419), 192–200 (2012).

18. S. H. Lee, M. Choi, T.-T. Kim, S. Lee, M. Liu, X. Yin, H. K. Choi, S. S. Lee, C.-G. Choi, S.-Y. Choi, X. Zhang, and B. Min, "Switching terahertz waves with gate-controlled active graphene metamaterials," *Nat. Mater.* **11**(11), 936–941 (2012).
19. B. Sensale-Rodriguez, T. Fang, R. Yan, M. M. Kelly, D. Jena, L. Liu, and H. Xing, "Unique prospects for graphene-based terahertz modulators," *Appl. Phys. Lett.* **99**(11), 113104 (2011).
20. P. Weis, J. L. Garcia-Pomar, and M. Rahm, "Towards loss compensated and lasing terahertz metamaterials based on optically pumped graphene," *Opt. Express* **22**(7), 8473–8489 (2014).
21. B.-H. Huang, W.-B. Lu, X.-B. Li, J. Wang, and Z.-G. Liu, "Waveguide-coupled hybrid plasmonic modulator based on graphene," *Appl. Opt.* **55**(21), 5598–5602 (2016).
22. Y. Wang, T. Li, and S. Zhu, "Graphene-based plasmonic modulator on a groove-structured metasurface," *Opt. Lett.* **42**(12), 2247–2250 (2017).
23. F. Chen, "A tunable high-efficiency optical switch based on graphene coupled photonic crystals structure," *J. Mod. Opt.* **64**(15), 1531 (2017).
24. B.-H. Shahram, G. Rahim, and H. S. Mohammad, "Three-dimensional analysis of an ultrashort optical cross-bar switch based on a graphene plasmonic coupler," *J. Lightwave Technol.* **35**(11), 2211–2217 (2017).
25. Y. Gao, G. Ren, B. Zhu, L. Huang, H. Li, B. Yin, and S. Jian, "Tunable plasmonic filter based on graphene splitting," *Plasmonics* **11**(1), 291–296 (2016).
26. Z.-X. Jia, Y. Shuai, S.-D. Xu, and H.-P. Tan, "Graphene-based tunable metamaterial filter in infrared region," *Smart Science* **4**(3), 127–133 (2016).
27. A. Andryieuski and A. V. Lavrinenko, "Graphene metamaterials based tunable terahertz absorber: effective surface conductivity approach," *Opt. Express* **21**(7), 9144–9155 (2013).
28. B. Z. Xu, C. Q. Gu, Z. Li, and Z. Y. Niu, "A novel structure for tunable terahertz absorber based on graphene," *Opt. Express* **21**(20), 23803–23811 (2013).
29. B. Janaszek, A. Tyszka-Zawadzka, and P. Szczepański, "Tunable graphene-based hyperbolic metamaterial operating in SCLU telecom bands," *Opt. Express* **24**(21), 24129–24136 (2016).
30. A. Khavasi, "Design of ultra-broadband graphene absorber using circuit theory," *J. Opt. Soc. Am. B* **32**(9), 1941–1946 (2015).
31. R. Alaei, M. Farhat, C. Rockstuhl, and F. Lederer, "A perfect absorber made of a graphene micro-ribbon metamaterial," *Opt. Express* **20**(27), 28017–28024 (2012).
32. L. Meng, D. Zhao, Z. Ruan, Q. Li, Y. Yang, and M. Qiu, "Optimized grating as an ultra-narrow band absorber or plasmonic sensor," *Opt. Lett.* **39**(5), 1137–1140 (2014).
33. Y.-L. Liao, Y. Zhao, X. Zhang, and Z. Chen, "An ultra-narrowband absorber with a compound dielectric grating and metal substrate," *Opt. Commun.* **385**, 172–176 (2017).
34. Y.-L. Liao and Y. Zhao, "An ultra-narrowband absorber with a dielectric-dielectric-metal structure based on guide-mode resonance," *Opt. Commun.* **382**, 307–310 (2017).
35. J. J. Greffet, R. Carminati, K. Joulain, J. P. Mulet, S. Mainguy, and Y. Chen, "Coherent emission of light by thermal sources," *Nature* **416**(6876), 61–64 (2002).
36. M. G. Moharam, T. K. Gaylord, E. B. Grann, and D. A. Pommet, "Formulation for stable and efficient implementation of the rigorous coupled-wave analysis of binary gratings," *J. Opt. Soc. Am. A* **12**(5), 1068–1076 (1995).
37. I. H. Malitson, "A redetermination of some optical properties of calcium fluoride," *Appl. Opt.* **2**(11), 1103–1107 (1963).
38. G. W. Hanson, "Dyadic Green's functions and guided surface waves for a surface conductivity model of graphene," *J. Appl. Phys.* **103**(6), 064302 (2008).
39. H. Li, L. Wang, and X. Zhai, "Tunable graphene-based mid-infrared plasmonic wide-angle narrowband perfect absorber," *Sci. Rep.* **6**(1), 36651 (2016).
40. Y. Zhang, T. Li, Q. Chen, H. Zhang, J. F. O'Hara, E. Abele, A. J. Taylor, H. T. Chen, and A. K. Azad, "Independently tunable dual-band perfect absorber based on graphene at mid-infrared frequencies," *Sci. Rep.* **5**(1), 18463 (2015).
41. B. Vasić and R. Gajić, "Graphene induced spectral tuning of metamaterial absorbers at mid-infrared frequencies," *Appl. Phys. Lett.* **103**(26), 261111 (2013).
42. H. Meng, L. Wang, G. Liu, X. Xue, Q. Lin, and X. Zhai, "Tunable graphene-based plasmonic multispectral and narrowband perfect metamaterial absorbers at the mid-infrared region," *Appl. Opt.* **56**(21), 6022–6027 (2017).
43. J. Hao, L. Zhou, and M. Qiu, "Nearly total absorption of light and heat generation by plasmonic metamaterials," *Phys. Rev. B* **83**(16), 165107 (2011).

## 1. Introduction

Perfect absorbers with engineered nanostructures have attracted a great deal of research interest due to their extensive applications in sensing [1], wavelength selective thermal emission [2], solar energy [3], cloaking [4] and photo-detection [5]. A variety of absorbers have been proposed and demonstrated at different frequencies including microwave [6,7], terahertz [8,9], infrared [10,11], and visible regions [12–14]. However, the fixed absorption peaks of these absorbers will make their function invalid when the application requirements

of absorption peaks change. In addition, fabrication of a new absorber to achieve another resonant absorption peak is not a cost-effective option. Thus, to conveniently meet the dynamic demand of different absorption peaks, it is very necessary to develop tunable absorbers.

Graphene, which consists of a single atomic layer of carbon with a 2-dimensional hexagonal lattice structure, has attracted intense scientific interests due to its unprecedented properties such as high electron mobility, high optical transparency, flexibility, and tunable conductivity [15–20]. One of the most interesting properties of graphene is that the conductivity can be tuned by applying the bias voltage upon graphene. Such characteristic of the voltage-control conductivity has enabled graphene act as a core component in designing various devices such as modulators [21,22], switches [23,24], tunable filters [25,26], and tunable absorbers [27,28]. To date, many graphene-based tunable absorbers have been presented, their operating bandwidths range from a single narrow-band to multiband and broadband [29–31]. However, a tunable absorber with absorption bandwidth less than 1.0nm has not been reported. On the other hand, it is noticed that some efforts have been made to achieve the ultra-narrowband absorbers because they can be applied as high temporal coherent thermal resources or high figure-of-merit sensors [32–35]. Therefore, considering the advantages of graphene and the ultra-narrowband absorbers, a graphene-based tunable ultra-narrowband absorber will be very desirable.

In this paper, we report a graphene-based tunable ultra-narrowband mid-infrared TE-polarization absorber. The tunable wavelength range of absorption peaks can reach 24.8nm by increasing the graphene's Fermi energy from 0.2eV to 1.0eV. In addition, the full width half maximums (FWHMs) under different  $E_f$  are less than 1.0nm. This tunable ultra-narrowband mid-infrared absorber has potential applications in the tunable filtering and tunable coherent emission of thermal source.

## 2. Structure

Figure 1 shows the proposed structure. The top layer is a dielectric grating which can be described by period  $p$ , ridge width  $w$ , and height  $h$ . The grating filled factor can be defined as  $f = w/p$ . Under the dielectric grating, there are two dielectric film layers separated by graphene. The thicknesses of these dielectric film layers are  $t_1$  and  $t_2$ . The substrate material is metal to efficiently block light from transmission. A TE-polarization plane electromagnetic wave  $\lambda$  is incident upon the proposed structure at an angle of  $\theta$  ( $90^\circ > \theta \geq 0^\circ$ ). The absorption characteristics of this proposed structure are evaluated with the rigorous coupled-wave analysis (RCWA) [36], and the absorption can be attained with  $A = 1 - R - T$  where  $R$  and  $T$  are the reflection and transmission, respectively. In addition, the metallic substrate is much larger than the penetration depth of incident electromagnetic waves so that  $T$  can be treated as zero. Thus, the absorption can be simplified with  $A = 1 - R$ . Calcium fluoride is used as dielectric material in the proposed structure, and the refractive index of calcium fluoride in the mid-infrared regime is described with formula [37]:

$$n_{CaF_2} = \sqrt{1 + \frac{0.5675888\lambda^2}{\lambda^2 - 0.050263605^2} + \frac{0.4710914\lambda^2}{\lambda^2 - 0.1003909^2} + \frac{3.8484723\lambda^2}{\lambda^2 - 34.649040^2}}. \quad (1)$$

Gold is material of metal substrate, and its permittivity can be expressed with a Drude model:

$$\epsilon_{Au} = 1 - \frac{\omega_p^2}{\omega(\omega + i\omega_c)} \quad (2)$$

where  $\omega$  is the angular frequency of the incident light,  $\omega_p = 1.32 \times 10^{16} \text{ rad/s}$ , and  $\omega_c = 1.2 \times 10^{14} \text{ rad/s}$ .

The surface conductivity  $\sigma_s$  of graphene permittivity can be derived from the Kubo formula [38] and can be given by:

$$\sigma_s = \frac{2e^2 k_B T}{\pi \hbar^2} \frac{i}{i\tau^{-1} - \omega} \ln \left[ 2 \cosh \left( \frac{E_f}{2k_B T} \right) \right] + \frac{ie^2}{4\pi\hbar} \ln \left[ \frac{2E_f + \hbar(\omega - i\tau^{-1})}{2E_f - \hbar(\omega - i\tau^{-1})} \right] \quad (3)$$

where  $e$  is the electron charge,  $\hbar = h/2\pi$  is the reduced Planck's constant,  $k_B$  is Boltzmann's constant,  $T$  is the temperature,  $E_f$  is the Fermi energy and  $\tau$  is the relaxation time. We set  $T = 300K$  and  $\tau = 1\text{ps}$  in this work. The refractive index of graphene can be expressed as  $n_g = \sqrt{1 - i\sigma_s/(\omega\epsilon_0 t_g)}$ , where  $t_g = 0.34\text{nm}$  is the approximate thickness of graphene,  $\epsilon_0$  is the vacuum permittivity.

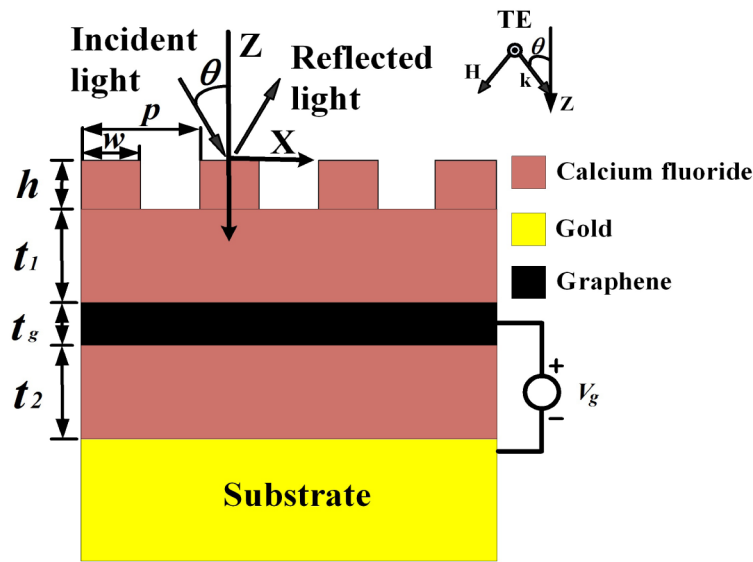


Fig. 1. Geometry of the grapheme-based tunable absorber structure

### 3. Results and discussion

Figure 2 shows the absorption spectra with different  $E_f$  at normal incidence, and the optimized structure parameters are  $p = 4.000\mu\text{m}$ ,  $f = 0.5$ ,  $t_1 = 4.000\mu\text{m}$ ,  $t_2 = 4.000\mu\text{m}$ , and  $h = 0.330\mu\text{m}$ . As illustrated in Fig. 2(a), by increasing the graphene's Fermi level from 0.2eV to 1.0eV, the absorption peaks blue-shift from  $5.43896\mu\text{m}$  to  $5.41418\mu\text{m}$ , and the tunable range of absorption peaks is 24.8nm. In addition, under different  $E_f$ , the absorption rate is still larger than 0.99. From Figs. 2(b)-2(d), the full width half maximums (FWHMs) under the different  $E_f$  are less than 1.0nm which is at least two orders lower than those of mid-infrared absorbers reported in [39–42]. The results indicate that the absorption peaks of the proposed structure can be tuned with ultra-narrow bandwidth by adjusting the graphene's Fermi level. Such tunable ultra-narrowband absorber can be used as a filter or coherent emission resource.

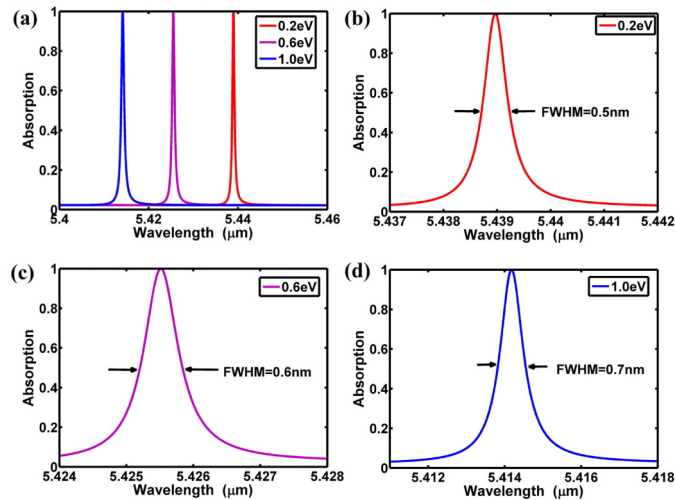


Fig. 2. (a) Absorption spectra with different Fermi level, (b) absorption spectrum with  $E_f = 0.2\text{eV}$ , (c) absorption spectrum with  $E_f = 0.6\text{eV}$ , (d) absorption spectrum with  $E_f = 1.0\text{eV}$ .

To get the ultra-narrowband absorption mechanism, Fig. 3 shows the electric field  $|E|$  within two unit cells at the absorption peak ( $\lambda = 5.43896\mu\text{m}$ ). The parameters used are the same with those in Fig. 2(b). From Fig. 3 we can see an obvious standing wave profile in X direction which indicates the guided-mode resonance in the dielectric material layers and graphene. In addition, as shown in Fig. 3, the electric field is mainly distributed in the lossless dielectric material so that the low power loss will occur in the resonance [43]. Furthermore, such low power loss, which results in a high quality factor, eventually produces an ultra-narrow bandwidth in our absorber. Therefore, we can ascribe the ultra-narrowband absorption of our absorber to the low power loss in the guided-mode resonance.

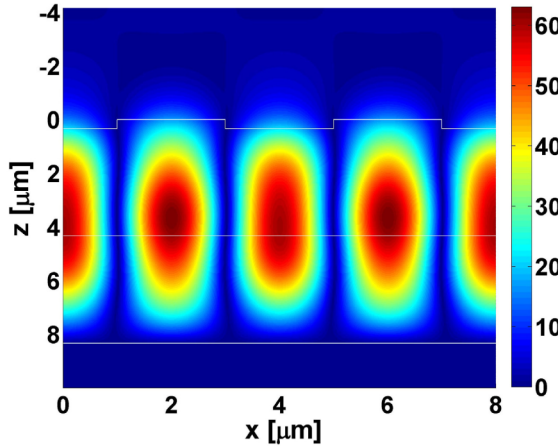


Fig. 3. Electric field distribution for  $\lambda = 5.43896\mu\text{m}$

To reveal the tuning mechanism of the ultra-narrowband absorber, we plot the real and imaginary parts of graphene permittivity as a function of wavelength in Fig. 4. As illustrated in Fig. 4, the real and imaginary parts of graphene permittivity slightly change in the

wavelength range from  $5.3\mu m$  and  $5.5\mu m$  under the same  $E_f$ . In contrast, the real and imaginary parts obviously jump when the graphene's Fermi level varies from  $0.2eV$  to  $1.0eV$  under the same wavelength. Furthermore, from Fig. 4, we can see the change of the real part under different Fermi levels is much larger than that of the imaginary part. Thus, the spectral shift may be mainly originated from the change of real part of graphene permittivity. According to the perturbation theory of Fabry-Perot cavity in Z direction, the spectral shift  $\Delta\lambda$  can be expressed with

$$\Delta\lambda = \lambda\Delta\epsilon \frac{\Delta V}{V} \quad (4)$$

where  $\Delta\epsilon$  is the change of the real part of the permittivity,  $\Delta V$  is the volume of grapheme,  $V$  is the volume of dielectric layers and  $\lambda$  is the center wavelength of spectral shift. By setting  $\lambda = 5.4\mu m$  and  $\Delta\epsilon \approx 300$ , we can get  $\Delta\lambda \approx 70nm$  which is on the same order with the results in Fig. 2.

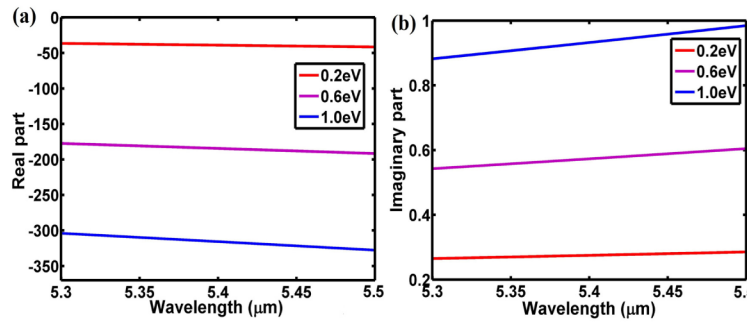


Fig. 4. Graphene permittivity as a function of wavelength with different Fermi level; (a) real part, (b) imaginary part.

To further verify the contribution of the real and imaginary parts of graphene permittivity, we calculate the absorption spectra with some special graphene permittivity. According to Eq. (3), the permittivities at  $\lambda = 5.43896\mu m$  with  $E_f = 0.2eV$  and  $E_f = 1.0eV$  are  $\epsilon_g = -40.02 + 0.2788*i$  and  $\epsilon_g = -320.3 + 0.9525*i$ , respectively. To clearly evaluate the independent contribution of the real and imaginary parts, the real and imaginary parts of graphene permittivity with  $E_f = 0.2eV$  are modified separately. All parameters employed in the following part of this paper are the same with those used in Fig. 2(b) if they are not specified. Figure 5 shows the absorption spectra with the special graphene permittivity. The blue solid curve in Fig. 5 is the absorption spectrum with  $\epsilon_g = -320.3 + 0.2788*i$  whose real part is equal to that with  $E_f = 1.0eV$ . In addition, the black solid curve in Fig. 5 is the absorption spectrum with  $\epsilon_g = -40.02 + 0.9525*i$  whose imaginary part is equal to that with  $E_f = 1.0eV$ . To compare the spectral shift, the absorption spectrum with  $\epsilon_g = -40.02 + 0.2788*i$  also shows in Fig. 5 with the red dashed curve. As shown in Fig. 5, the spectral shift of the blue solid curves is 25.0nm. However, the black solid curve and red dashed curve are almost overlapping so that the spectral shift of the black solid curve is almost negligible. To directly show the contribution of the real part of permittivity, we plot the absorption spectrum shown as green dashed curve with  $\epsilon_g = -320.3$  whose imaginary part is 0. The green dashed curve and blue solid curve are also almost overlapping. Thus, Fig. 5 shows that the spectral shift originated from the change of real part of graphene permittivity

is much larger than that originated from the change of imaginary part. We can conclude that the spectral shift is mainly attributed to the change of the real part of the graphene's permittivity.

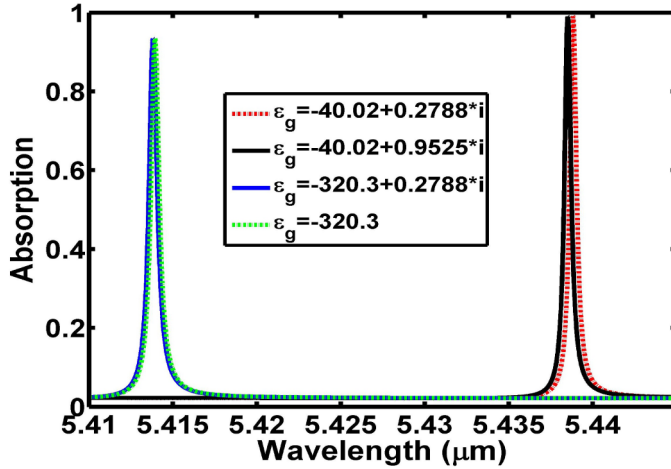


Fig. 5. Absorption spectra with different graphene permittivity.

In our graphene-based tunable ultra-narrowband mid-infrared absorber, both gold and graphene have imaginary parts of permittivity which can result in absorption. In order to clarify the contribution of gold and graphene on the perfect absorption in our absorber, the power loss of gold and graphene will be evaluated. The power loss for a nonmagnetic dispersive medium can be described by

$$P = \int \frac{1}{2} \epsilon_0 \omega \text{Im} \epsilon(\omega) |E|^2 dV \quad (5)$$

where  $\text{Im} \epsilon(\omega)$  is the imaginary part of permittivity [43]. We calculate the power loss of gold and graphene at the absorption peak  $\lambda = 5.43896 \mu\text{m}$  which is shown in Fig. 2(b) with  $E_f = 0.2 \text{ eV}$ . We define  $|E|_{Au}$  and  $|E|_g$  as the electric field in gold and graphene, respectively. Based on the data of  $|E|$  extracted from Fig. 3, we can achieve

$$\frac{P_{Au}}{P_g} = \frac{\text{Im} \epsilon_{Au}(\omega)}{\text{Im} \epsilon_g(\omega)} \cdot \frac{\int |E|_{Au}^2 dV}{\int |E|_g^2 dV} \approx \frac{448.95}{0.2788} \cdot \frac{600}{250000} \approx 4 \quad (6)$$

where  $P_{Au}$  and  $P_g$  are the power loss of gold and graphene, respectively. From Eq. (6), we can see that the power loss of gold is about 4 times as large as that of graphene. We also calculate the power loss of gold and graphene at the absorption peak  $\lambda = 5.41418 \mu\text{m}$  which is shown in Fig. 2(d) with  $E_f = 1.0 \text{ eV}$ . By employing the same method, we can get  $\frac{P_{Au}}{P_g} \approx 1$ .

From the above discussion, we can see that the contribution of gold and graphene on perfect absorption is in the same order of magnitude in our absorber when the graphene's Fermi level is tuned from 0.2eV to 1.0eV.

Next, we investigate the influence of the geometric parameters on the absorption characteristic. In addition, without loss of generality, the graphene's Fermi energy is set as 0.2eV. We simulate the absorption spectra with different filled factors, grating heights, and dielectric layer thicknesses in Fig. 6. As shown in Fig. 6(a), the absorption will decrease if the filled factor deviates from 0.5, but it is still larger than 0.9 in the filled factor range from 0.3

to 0.7. As seen in Fig. 6(b), the absorption peak will red-shift with the increasing grating height. The absorption rate is above 0.98 in the grating height range from  $0.30\mu m$  and  $0.36\mu m$ . Figure 6(c) shows that the absorption peaks will red-shift if the dielectric layer thickness  $t_1$  increases. The absorption rate is above 0.9 when  $t_1$  range from  $3.950\mu m$  and  $4.050\mu m$ . In addition, we can see the similar results in Fig. 6(d) with those in Fig. 6(c).

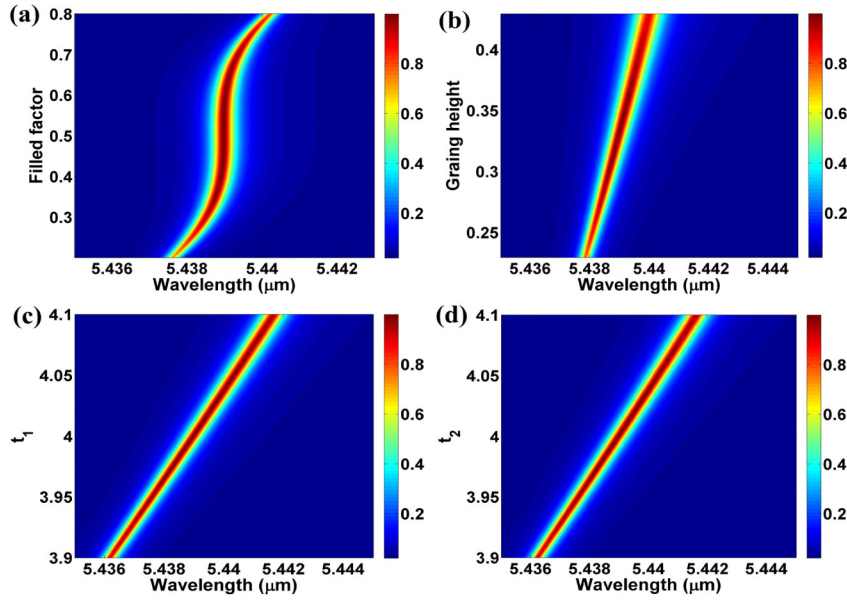


Fig. 6. (a) Absorption spectra with different filled factor, (b) absorption spectra with different grating height, (c) absorption spectra with different  $t_1$ , (d) absorption spectra with different  $t_2$ .

To show the influence of refractive indices of the dielectric material to our absorber, the absorption spectra with different refractive indices are shown in Fig. 7. The refractive index of dielectric material is defined with  $n$ . Other parameters employed in the simulation process are the same with those used in Fig. 2(b). As seen in Fig. 7, the absorption peaks with near-perfect absorption will red-shift if  $n$  increases. The red-shift phenomenon in Fig. 7 can be explained with the guided-mode resonance mechanism shown in Fig. 3. As the refractive index of the dielectric material increases, the resonance peaks shift to longer wavelengths to support the guided mode in the dielectric material and graphene. The absorption peaks of TE<sub>1</sub> mode at  $5.842\mu m$  and  $6.0255\mu m$  are also shown in Fig. 7. The mode profiles of TE<sub>0</sub> and TE<sub>1</sub> mode with  $n=1.65$  are inserted in Fig. 7. In addition, Fig. 7 indicates that the absorption peaks can be shifted by replacing the dielectric material.

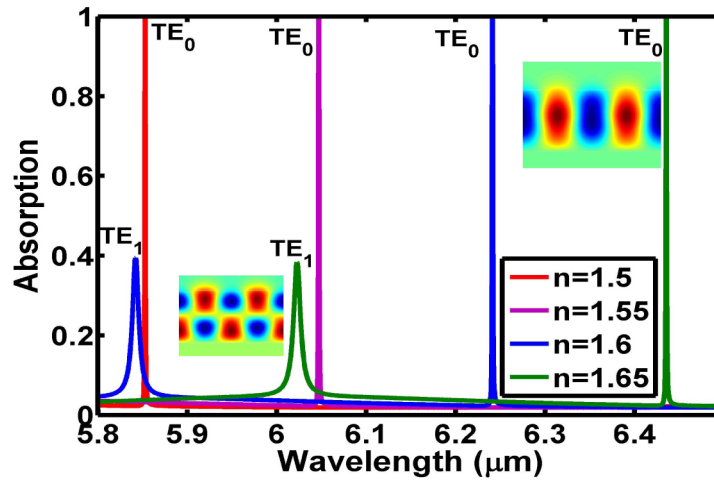


Fig. 7. Absorption spectra with different refractive indices of the dielectric material. The insert shows the electric-field distribution at the resonant absorption wavelengths of  $6.0255\mu\text{m}$  and  $6.4355\mu\text{m}$ .

To investigate how the absorption is affected by the incident angles, the absorption spectra with different incident angles are simulated in Fig. 8. As shown in Fig. 8, the absorption peaks red-shift with the increasing incident angles. In addition, the absorption peaks of  $\text{TE}_1$  and  $\text{TE}_2$  modes can be seen when  $\theta$  increases in the interesting wavelength range. The mode profiles of different absorption peaks with  $\theta = 30^\circ$  are inserted in Fig. 8.

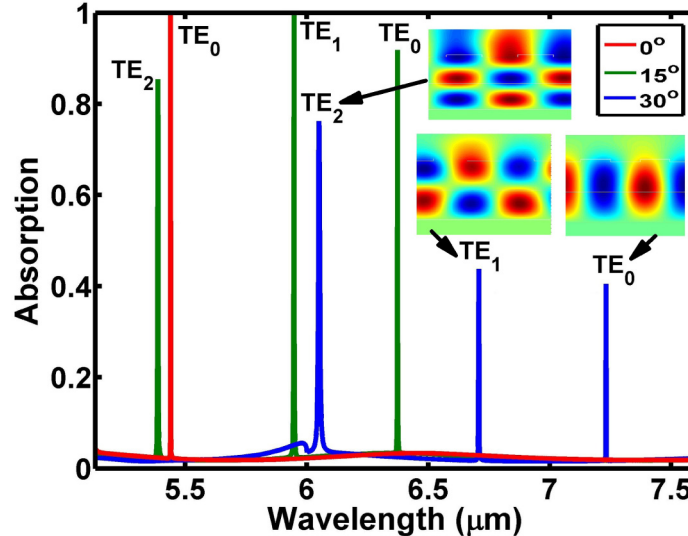


Fig. 8. Absorption spectra with different incident angles. The insert shows the electric-field distribution at the resonant absorption peaks with  $\theta = 30^\circ$ .

We notice that the absorption bandwidth is less than 1.0nm which indicates our absorber has high temporal coherence if it is applied as a thermal emitter resource [35]. However, the spatial coherence is another important feature to a thermal emitter resource. To investigate the spatial coherence, we plot the angle-resolved absorption at the incident wavelength of  $5.43896\mu\text{m}$  in Fig. 9(a). Figure 9(a) shows that the absorption at  $\theta = 0^\circ$  is larger than 0.99.

The angular width of FWHM with  $\Delta\theta$  is used to describe the angle-resolved absorption characteristics. To clearly show the angle-resolved absorption characteristics, Fig. 9(b) is plotted to show the zoom-in pattern around  $\theta = 0^\circ$ . In Fig. 9(b),  $\Delta\theta$  at  $\theta = 0^\circ$  is less than  $0.16mrad$  which means that our absorber is a highly directional thermal emitter. The corresponding spatial coherence length is as large as  $\lambda/\Delta\theta = 34.2mm$  which is much larger than the corresponding wavelength. Thus, our absorber has both high temporal coherence and high spatial coherence.

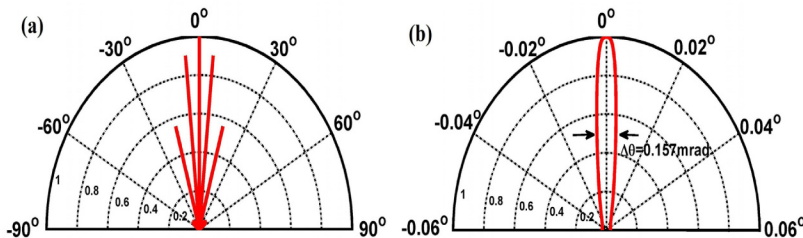


Fig. 9. (a) Absorption angular pattern at  $\lambda = 5.43896 \mu m$ , (b) absorption angular pattern around  $\theta = 0^\circ$ .

#### 4. Conclusion

We report a graphene-based tunable ultra-narrowband mid-infrared TE-polarization absorber in this paper. The absorption peak can be tuned by tuning the graphene Fermi level. Furthermore, the absorption bandwidth is less than  $1.0nm$  and the absorption rate is more than  $0.99$  in the tuning wavelength range. The ultra-narrowband absorption mechanism is originated from the low power loss in the guided-mode resonance. The tuning function is mainly attributed to the change of the real part of the graphene's permittivity. This tunable ultra-narrowband mid-infrared absorber has potential applications in the tunable filtering and tunable coherent emission of thermal source.

#### Funding

Anhui Provincial Natural Science Foundation (No. 1508085MF136).